

Projection of future heatwaves in the Pearl River Delta through CMIP6-WRF dynamical downscaling

Ziping Zuo¹, Jimmy Chi-Hung Fung¹, Zhenning Li¹, Yiyi Huang¹, Mau Fung Wong¹, Alexis Kai-Hon Lau¹, and Xingcheng Lu¹

¹Affiliation not available

August 11, 2023

Ziping Zuo^a, Jimmy C.H. Fung^{a,b}, Zhenning Li^{a,*}, Yiyi Huang^d, Mau Fung, Wong^a, Alexis K.H. Lau^{a,c}, Xingcheng Lu^e

^a *Division of Environment and Sustainability, The Hong Kong University of Science and Technology, Clear Water Bay, Hong Kong, China*

^b *Department of Mathematics, The Hong Kong University of Science and Technology, Clear Water Bay, Hong Kong, China*

^c *Department of Civil and Environmental Engineering, The Hong Kong University of Science and Technology, Clear Water Bay, Hong Kong, China*

^d *Department of Hydrology and Atmospheric Sciences, University of Arizona, Tucson, AZ, USA*

^e *Department of Geography and Resource Management, The Chinese University of Hong Kong, Shatin, Hong Kong, China*

Corresponding author: Zhenning Li, lzhenn@ust.hk

ABSTRACT

Recent worldwide heatwaves have shattered temperature records in many regions. In this study, we applied a dynamical downscaling method on the high-resolution version of the Max Planck Institute Earth System Model (MPI-ESM-1-2-HR) to obtain projections of the summer thermal environments and heatwaves in the Pearl River Delta (PRD) considering three shared socioeconomic pathways (SSP1-2.6, SSP2-4.5, and SSP5-8.5) in the middle and late 21st century. Results indicated that relative to the temperatures in the 2010s, the mean increases in the summer (June–September) daytime and nighttime temperatures in the 2040s will be 0.7–0.8 °C and 0.9–1.1 °C, respectively. In the 2090s, the mean difference will be 0.5–3.1 °C and 0.7–3.4 °C, respectively. SSP1-2.6 is the only scenario in which the temperatures in the 2090s are expected to be lower than those in the 2040s. Compared with those in the 2010s, hot extremes are expected to be more frequent, intense, extensive, and longer-lasting in the future in the SSP2-4.5 and SSP5-8.5 scenarios. In the 2010s, a heatwave occurred in the PRD lasted for 6 days on average, with a mean daily maximum temperature of 34.4 °C. In the 2040s, the heatwave duration and intensity are expected to increase by 2–3 days and 0.2–0.4 °C in all three scenarios. In the 2090s, the increase in these values will be 23 days and 36.0 °C in SSP5-8.5. Moreover, a 10-year extreme high temperature in the 2010s is expected to occur at a monthly frequency from June to September in the 2090s.

SIGNIFICANCE STATEMENT

Pearl River Delta (PRD) has been experiencing record-shattering heatwaves in recent years. This study aims

to investigate the future trends of summer heatwaves in the PRD by modeling three future scenarios including a sustainable scenario, an intermediate scenario, and a worst-case scenario. Except the sustainable scenario, summer temperatures in the intermediate and worst-case scenarios will keep increasing, and heatwaves will become more frequent, intense, extensive, and longer-lasting. In the worst-case scenario, extreme heat events that occurred once in 10 years in the 2010s will shorten to once a month in the 2090s. A better understanding of heatwave trends will benefit implementing climate mitigation methods, urban planning, and improving social infrastructure.

1. Introduction

Greenhouse gases (GHGs) have been warming the atmosphere, land, and ocean since Industrial Revolution, and each decade in the last 40 years has been warmer than any previous decades since 1850 (IPCC 2021). According to the Sixth Assessment Report (AR6) of the Intergovernmental Panel on Climate Change (IPCC), the global land surface temperature in 2011–2020 was 1.6 °C higher than that in 1850–1900. The characteristics of extreme weather and climate events are projected to change in response to the warming climate. Extreme hot temperature events are expected to occur more frequently and intensely with global warming. Compared with that in 1850–1900, global terrestrial 10-year extreme heat events are expected to occur 3.1 times more frequently, with an intensity that is 1.9 °C higher, if the global warming level reaches 1.5 °C (IPCC 2021).

The present study is focused on heatwaves, as a type of extremely high-temperature event. Heatwaves typically refer to a prolonged period of excessively hot days, although no universal definition is available. Heatwaves are usually defined in terms of absolute or relative criteria. According to an absolute criterion, a heatwave is defined as a prolonged period with daily maximum temperatures exceeding a fixed value (e.g., 35 °C) (Wang et al. 2017). According to a relative criterion, a heatwave is a prolonged period with daily maximum temperatures exceeding a certain percentile (e.g., the 90th percentile) for a long-term temperature histogram (Ding et al. 2010). The present study adopts the Hong Kong Observatory’s threshold for defining a heatwave event (daily maximum temperature exceeding 33 °C for at least three days) using an absolute criterion. This definition is based on the humid and hot subtropical climate in the Pearl River Delta (PRD), which is the target area of this research. Moreover, Chan et al. (2011) highlighted that help-seeking behaviors are expected to intensify when the temperature rises to 30–32 °C. For a regional heatwave analysis, the frequency, intensity, and duration of a heatwave event can be represented by metrics such as the hot day frequency (Yang et al. 2017), heatwave frequency (Perkins and Alexander 2013), heatwave duration (Perkins et al. 2012), heatwave temperature (Perkins 2015), very hot day hours (Shi et al. 2019), and nighttime heatwaves (Thomas et al. 2020).

Heatwaves can adversely influence human health, ecological environment, social infrastructure, and the overall economy. Specifically, intense heatwaves can increase human morbidity and mortality. Heat-related illnesses include heat cramps, exhaustion, and stroke. Females, the elderly, and people engaged in physical work in outdoor environments are more vulnerable to extreme heat (Ebi et al. 2021). In the summer of 2003, Europe experienced the hottest heatwave recorded since 1540, which led to the death of 70,000 people (Robine et al. 2008). Many countries in the northern hemisphere suffered severe heatwaves in 2010, including China, European continent, North Africa, the United States, and Russia. In Russia, over 55,000 people died during the heatwave (Horton et al. 2016). In 2022, record-breaking heatwaves swept through Europe, South America, India, and China, killing more than 12,000 people. Heatwaves can also exacerbate wildfires and drought. In the hot and dry meteorological conditions induced by extreme heat, the vegetation becomes devoid of moisture and can fuel wildfires that can spread extensively and burn for considerable periods. The emergence of more frequent and intense heatwaves burdens the social infrastructure, such as healthcare, power supply, and agriculture. For example, railway tracks may buckle, and roofs may melt at high temperatures. Additionally, heatwaves can deteriorate the labor productivity and overall economy, especially in low- and low-middle-income countries (Chavaillaz et al. 2019). For every trillion tons of carbon emissions, the global annual productivity loss is expected to increase by 3% and 3.6% of the total GDP in representative concentration pathway (RCP) scenarios RCP4.5 and RCP8.5, respectively (Chavaillaz et al. 2019).

Spatial heterogeneity exists in the occurrence of heatwaves. For example, studies have found that heatwaves are more frequent and intense in urban areas compared to rural areas due to urbanization, with urban areas contributing over 45% to heatwaves in southwestern, northern, and southern China (Wu et al. 2020). The frequency and intensity of heatwaves also vary greatly between regions and climatic zones, depending on factors such as latitude and altitude. For instance, during heatwaves, the Yangtze River and the Beijing-Tianjin-Hebei region experience 'very hot' thermal comfort levels, which have been attributed to the movement of the sub-high-pressure belt to the Yangtze River area in summer. On the other hand, the southwest of Tibet, which is at higher altitudes, has the lowest thermal index despite their proximity to lower latitudes (Wu et al. 2022). Considerable research has been performed to project future heatwave trends on both the global and regional scales using climate models. By the end of this century, in business-as-usual scenarios, heatwaves as severe as the Russian heatwave in 2010 will become the norm and are projected to occur every two years in regions such as southern Europe, North America, and Indonesia (Russo et al. 2014). Projections for China show that regions such as Yangtze River and Southern China, which suffered from heatwaves in previous climate conditions, will experience more frequent and severe heatwaves under global warming (Guo et al. 2017; Wang et al. 2017).

To better respond and adapt to changes in future extreme climate events, IPCC AR6 established five new illustrative future climate scenarios, i.e., shared socioeconomic pathways (SSPs): SSP1-1.9, SSP1-2.6, SSP2-4.5, SSP3-7.0, and SSP5-8.5. The numbers represent the combination of SSPs and RCPs, representing radiative forcing values of $1.9 \text{ W}\cdot\text{m}^{-2}$, $2.6 \text{ W}\cdot\text{m}^{-2}$, $4.5 \text{ W}\cdot\text{m}^{-2}$, $3.7 \text{ W}\cdot\text{m}^{-2}$ and $8.5 \text{ W}\cdot\text{m}^{-2}$ to be achieved under different socioeconomic assumptions, climate mitigation levels, precursors of aerosols and non-methane ozone, and air pollution controls in the year 2100, respectively (IPCC 2021). These RCPs used in IPCC AR5 were replaced with these new future scenarios to provide a more comprehensive overview of different climate outcomes. In the present study, SSP1-2.6, SSP2-4.5, and SSP5-8.5, representing low, intermediate, and very high GHG emissions, respectively, were selected to explore future climate outcomes in the mid-term (2040–2049) and long term (2090–2099). In all emission scenarios, the global surface temperature is expected to keep increasing until at least mid-century, and global warming levels of 1.5 degC and 2 degC are expected to be exceeded by the end of this century unless the GHG levels significantly decrease. Compared with 1850–1900, the global mean surface temperature in 2081–2100 will potentially increase by 1.3–2.4 degC, 2.1–3.5 degC, and 3.3–5.7 degC in SSP1-2.6, SSP2-4.5, and SSP5-8.5, respectively.

Studies utilizing climate output data from the recently released phase 6 of the Coupled Model Intercomparison Project (CMIP6) are still limited, as CMIP5 data is currently more widely used. However, there is a need to update research using CMIP6 to improve our understanding of future climate scenarios. Compared with CMIP5, CMIP6 provides finer-resolution climate model data and a more comprehensive set of future pathways. In terms of extreme climate events, CMIP6 can capture spatiotemporal trend patterns (with the observations as reference) more accurately than CMIP5 (Fan et al. 2020; Chen et al. 2020). Therefore, there is a growing need to update future climate projections using CMIP6 output data. Typically, the resolution of global climate models (GCMs) ranges between 100 km and 600 km, which is too coarse for regional climate analyses. Several physical processes, such as those related to cloud microphysics, deep convections, as well as topographic drags, cannot be appropriately resolved using GCMs. Therefore, by using the dynamical downscaling method to explore regional heatwaves, we downscaled the resolution of GCM to 1 km on the PRD, which is one of the most densely urbanized and populated regions worldwide. Such urban regions are expected to suffer more from extreme heat events in the future compared with other regions (IPCC 2021).

This paper comprehensively describes the daytime and nighttime heatwave trends in the PRD region by the middle and end of the century under different emission pathways. The remaining paper is structured as follows: Section 2 describes the methods used and the heatwave metrics considered. Section 3 presents the results, and Section 4 presents the concluding remarks.

2. Data and Methodology

a. Dynamical downscaling method

A high-resolution version of the Max Planck Institute Earth System Model (MPI-ESM), MPI-ESM-1-2-HR, which corresponds to a 1.0deg x 1.0deg grid spacing and has an output interval of 6-hour, was used to set the initial and lateral boundary conditions to perform dynamical downscaling over the PRD due to its good representation of large-scale forcing and high spatial resolution. The model’s horizontal resolution of 100 km for the atmospheric component and 40 km for the ocean component rank high among CMIP6 models and can provide more accurate initial and boundary conditions for the regional model and better capture small-scale physical processes (Adachi and Tomita 2020). In the evaluation of the multi-models in CMIP5, MPI-ESM-MR, the antecedent version of MPI-ESM-1-2-HR, outperformed the other models in simulating the East Asian monsoon regions (Camargo 2013). MPI-ESM-1-2-HR in CMIP6 has higher resolution and complexity than its lower-resolution versions and has shown to have a well-balanced radiation budget and a better performance in atmospheric dynamic, such as mid-latitude storm track dynamics and atmospheric blocking (Muller et al. 2018; Xu et al. 2021; Han et al. 2022). Moreover, MPI-ESM-1-2-HR can effectively reproduce the temperature signals of the 20th century and has projected that the global warming level from 1850 to 2080–2100 will range from 1.5 degC in RCP2.6 to 4.4 degC in RCP8.5. The Weather Research and Forecasting (WRF) model was used as a nested regional model, driven by MPI-ESM-1-2-HR, to generate fine-resolution regional climate information pertaining to the PRD.

b. Land use change projection and refinement of urban geometric parameters

The default WRF assigns surface roughness length and background albedo values based on a single value for each land use category, which does not accurately reflect the complex urban geography of the PRD. This leads to degraded model simulations. To address this issue, we reassigned roughness length and albedo values for the 2010s using a combination of Baidu Maps, Hong Kong Planning department data, and the World Urban Database and Portal Tool (WUDAPT) level 0 method, which employs the Local Climate Zone (LCZ) classification system. The LCZ system includes 17 classifications, comprising 10 build-up types and 7 natural types (Bechtel et al. 2015; Stewart and Oke 2012). Then the LCZ categories with new set of roughness length and albedo were converted to fit the land use classifications of United State Geological Survey (USGS) land use system available in WRF (Fig. 1 (b), Fig. S1 (a), and (c)). Several studies have shown that this approach improves simulations of 2 m temperature and 10m wind speed (Liu 2020; Yeung et al. 2020). For the future land use projection, we only used the WUDAPT dataset provided by Chen’s group, which conducted LCZ simulations for 2050 using the Global Change Analysis Model (GCAM) and Future Land Use Simulation Model (FLUS) (Chen et al. 2021). The accuracy of this LCZ classification and simulation are assessed in their paper which confirms the reliability of the dataset. Thereafter similar steps of calculating roughness length and albedo were taken and the LCZ classifications were converted to fit WRF USGS land use category (Fig. 1 (c), Fig. S1 (b), and (d)). The land use parameters in the 2090s is assumed to be the same as the 2040s. These refinements improve the accuracy of the WRF model and enhance our ability to project land use change in the PRD.

c. Experimental design and model configuration

To capture the climate context of different scenarios and stages in the 21st century, two sets of time-slice simulations were conducted for the 2040s (2040–2049) and 2090s (2090–2099) in each of the three SSP emission scenarios, namely SSP1-2.6 (sustainability), SSP2-4.5 (middle of the road), and SSP5-8.5 (fossil-fueled development). To compare the present and future trends, baseline simulations were also performed for the 2010s (2011–2020) in the SSP2-4.5 scenario because it was assumed to be the closest pathway to reality for the 2010s. Additionally, simulations driven by the European Centre for Medium-Range Weather Forecasts Reanalysis data version 5 (ERA5) for 2011–2020 were performed for bias correction.

The WRF model version 3.9.1 was initiated on May 1 for each year of the two decades and integrated from May 1 to September 30, covering the complete warm season in southern China. The period from May 1 to May 31 was treated as the soil temperature and moisture spin-up stage, and the analysis period was from 1 June to 30 September. Vertical layers were implemented in 39 eta coordinates from the surface to the stratopause, with the planetary boundary layer corresponding to dense layers. Specifically, 20 layers were assigned from the surface to an altitude of approximately 2000 m above the terrain. The WRF model was

utilized to simulate atmospheric conditions at multiple spatial scales. The outermost domain, WRF D01, had a 27 km x 27 km horizontal resolution and covered a vast region spanning East and Southeast Asia, the South China Sea, and the tropical western Pacific. Nested within D01 was WRF D02, with a higher resolution of 9 km x 9 km, focused on southern China. WRF D03 covered the Guangdong province, while WRF D04, with a resolution of 1 km x 1 km, was used to capture fine-scale features over the PRD. To ensure accurate representation of the large-scale mean flow from MPI-ESM-1-2-HR, grid nudging was implemented in WRF D01 every six hours during model integration. The domain configuration is shown in Fig. 1 (a).

The planetary boundary layer physics was reflected by the Asymmetric Convective Model version 2 (ACM2) (Pleim 2007). The Unified Noah Land Surface Model (Noah LSM) was responsible for land surface. These two schemes are essential in modeling 2 m temperature for providing a vertical profile of the turbulent kinetic energy and its dissipation rate, and the surface energy budget, respectively. Xie et al. (2012), who quantified the sensitivity of surface variables (2 m temperature and 10m wind speed) to four PBL schemes in the WRF (ACM2, YSU, MYJ, and Boulac) in the Pearl River Delta show ACM2 produces the best simulation of 2 m temperature and 10m wind speed compared to observations. The cloud microphysics was reflected by the WRF single-moment 3-class scheme (Hong et al. 2004). The Kain–Fritsch scheme was implemented in WRF D01 and D02 to parameterize the cumulus convections (Kain 2004). The Rapid Radiative Transfer Model for General Circulation Models was the radiation transfer scheme for both longwave and shortwave processes (Mlawer et al. 1997). This set of WRF physics schemes was also employed in many other studies focusing on the Pearl River Delta (Yeung et al. 2020; Bhautmage et al. 2022). The WRF output was configured to have an hourly frequency to effectively archive the diurnal cycle feature over the PRD.

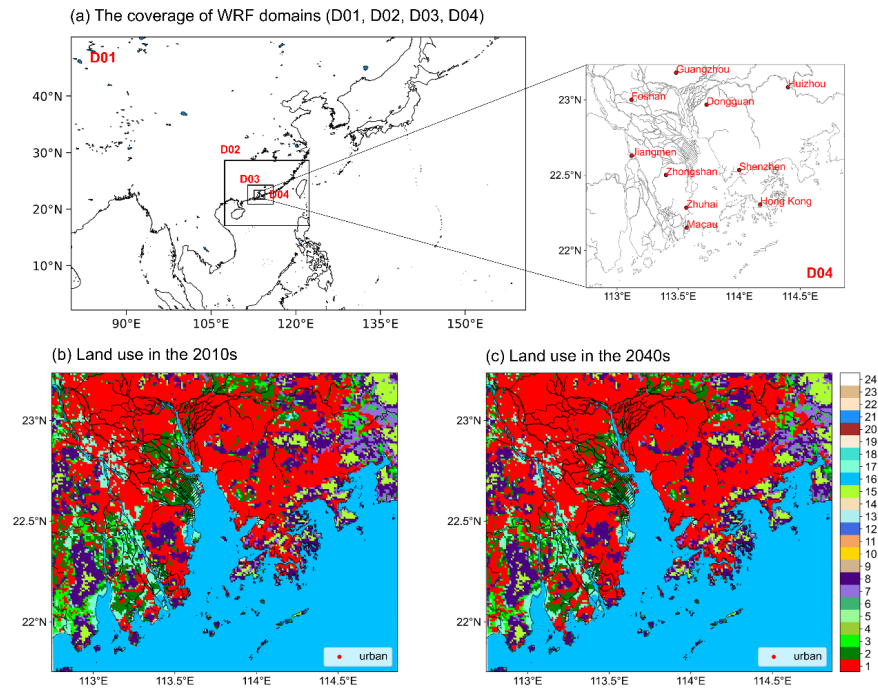


Fig. 1. (a) Horizontal coverage of WRF nested domains (resolution: 27 km for D01, 9 km for D02, 3 km for D03, 1 km for D04). D04 covers major cities and surrounding areas in the PRD. (b), (c) USGS 24-category land use in the 2010s, and 2040s. Red color denotes urban area. The explanation of other land use type is listed in Table S1. in the Supporting Material.

d. Heatwave definitions

We defined a very hot day as one with the daily maximum temperature exceeding 33 °C and a very hot night as one with the daily minimum temperature exceeding 28 °C (HKO 2022). A daytime heatwave event was defined as a period with at least three consecutive very hot days in a summer season spanning June to September. A nighttime heatwave event was considered to consist of at least three consecutive very hot nights.

We evaluated five heatwave indices (Table 1): hot day frequency (HDF), heatwave duration (HWD), heatwave temperature (HWT), hot night frequency (HNF), and nighttime heatwave duration (NHD). These indices can effectively represent the trends of magnitude, intensity, and duration of daytime and nighttime heatwaves. Moreover, the spatial plots of each index can reflect the spatial expansion of hot areas.

Table 1. Heatwave Index Definitions

Heatwave index	Definition	Unit
HDF	Mean number of very hot days each summer	Day/summer
HNF	Mean number of very hot nights each summer	Night/summer
HWD	Average duration of daytime heatwaves	Day/time
HND	Average duration of nighttime heatwaves	Night/time
HWT	Average daily maximum temperature during daytime heatwaves	°C

e. Return period definition

A return period is often considered in calculating the period of recurrence of extreme events such as earthquakes and floods. We applied this measure to extreme heat events. Unlike the definitions of heatwaves, we evaluated the highest hourly temperature in each grid cell from 2011 to 2020 as a 10-year extreme heat event. The highest temperature in each grid in the 2010s was used as a benchmark to calculate the return period of a 10-year extreme heat event in each scenario in future decades. The return period was calculated using Weibull’s formula (Horton et al. 2016).

$$\text{return period} = \frac{n+1}{m}$$

where n is the sample size, and m is the rank of the values in decreasing order. In this study, m is the descending order rank of the highest temperatures in the 2010s, 2040s and 2090s.

f. Validation and bias correction of the datasets

The ERA5-driven WRF output data in hourly sequence from 2011 to 2020 (ERA5-driven) and CMIP6-driven WRF output data in hourly sequence in the SSP2-4.5 scenario (CMIP6-driven) from the same period were used to correct the systematic biases of the 2 m temperature. The bias correction was based on SSP2-4.5 because it was assumed to be the closest pathway to reality for the 2010s.

Reanalysis data can reflect past weather and climate information and fill in the gaps associated with observation records and satellite data. Because they are spatially complete and consistent in time with observation records, reanalysis data can be effectively used for bias correction. The ERA5-driven and CMIP6-driven datasets corresponded to the same WRF configuration and physics parameterization for consistency. The correction value and corrected dataset were determined using the following two equations, respectively. Fig. S2 (b) shows the spatial map of the mean correction value. CMIP6 tend to overpredict and underpredict the 2 m temperature in inland and coastal areas, respectively, as depicted in Fig S2 (b).

$$\text{correction value} = \text{ERA5 driven dataset} - \text{CMIP6 driven dataset}$$

$$\text{corrected CMIP6 driven dataset} = \text{CMIP6 driven dataset} + \text{correction value}$$

The performance of the bias correction was evaluated using 2 m temperature observation data collected in the PRD between 2016 and 2020. This time frame was chosen as it provided a higher quality temperature dataset due to more complete data from observation stations compared to other periods. All three datasets were organized in hourly frequencies to achieve the best bias correction and evaluation performance. We selected 118 observation stations among which the percentage of missing values was less than 10%. See Fig. S3 in Supporting Information for the spatial distribution of these 118 observation stations.

The following statistical metrics were calculated to evaluate the bias correction performance: mean bias (MB), mean absolute error (MAE), root mean square error (RMSE), and index of agreement (IOA), which reflect the bias and absolute error between the corrected CMIP6 dataset and observations, standard deviation of the residuals, and accuracy of the corrected CMIP6 dataset, respectively. The metrics were calculated using the following equations.

$$\begin{aligned} \text{MAE} &= \frac{1}{n} \sum_1^n (|C_m - C_o|) \\ \text{MB} &= \frac{1}{n} \sum_1^n (C_m - C_o) \\ \text{RMSE} &= \sqrt{\frac{1}{n} \sum_1^n (C_m - C_o)^2} \\ \text{IOA} &= 1 - \frac{\sum_1^n (C_m - C_o)^2}{\sum_1^n (|C_m - C_o| + |C_o - C_m|)^2} \end{aligned}$$

where C_m is the simulation value in the grid closest to the station, C_o is the observation station value, and n is the number of observation stations, C_o is the mean value of the temperature at observation stations.

Validation result indicates that the ERA5-driven simulation tended to overestimate the 2 m temperature by 0.6 °C compared with the observations. The CMIP6-driven dataset overestimated the corresponding values more than the ERA5-driven dataset. Compared with ERA5, the CMIP6-driven dataset exhibited a larger RMSE and a smaller IOA, indicating inferior performance (see Table. S2 in Supporting Information). However, the bias was effectively reduced after correction, with the MB and RMSE decreasing and the IOA increasing. To precisely compare the simulations and observations, the difference associated with each observation station in the two datasets was evaluated. The CMIP6-driven simulations overpredicted the 2 m temperature at most observation stations, and this bias was effectively reduced after bias correction. The more accurate results obtained after bias correction provided a more solid basis for further analysis (see Fig. S5–S11 in Supporting Information).

Since the validation period is overlapped with the correction period, we also used the correction value from 2011 to 2015 to correct the original CMIP6-driven dataset from 2016 to 2020 and compared the performance of this five-year correction value with that of the ten-year correction value. The results (Fig. S2–S11) indicate that the difference between the two sets of correction values is marginal, with slightly better performance observed for the ten-year correction value. Therefore, to achieve better performance for current and future projections, the following results used the ten-year correction value obtained from the 2011–2020 period.

3. Results

a. Mean state of future thermal environment in different scenarios

1) Decadal mean 2 m temperature in the PRD

CMIP6-driven WRF hourly output data were used to calculate the mean 2 m temperature over the 2010s, 2040s, and 2090s in different scenarios. Simulations for the 2010s in the SSP2-4.5 scenario were treated as the baseline for comparison.

Fig. 2 shows the spatial pattern of the hourly mean 2 m temperature in different decades in the SSP2-4.5 scenario in the daytime (11:00 AM–4:00 PM, Local Standard Time (LST)) and nighttime (1:00 AM–6:00 AM, LST). The spatial mean values are summarized in the Table 2. SSP2-4.5 is the medium pathway of future GHG emissions, assuming the historical trend remains unchanged in the future. At present, the hourly mean 2 m temperature in the daytime over the land area of the PRD is 31.5 °C. This temperature is expected to increase by 0.7 °C and 1.5 °C in the 2040s and 2090s, respectively. The nighttime hourly mean 2 m temperature in the 2010s is 26.9 °C and is expected to increase by 0.9 °C and 1.8 °C in the 2040s and 2090s, respectively. The rate of increase of the nighttime temperature is higher than that of the daytime temperature. The larger increase in the nighttime temperature may be caused by the increase in absorbed downward longwave radiation and anthropogenic heat. The diurnal temperature range in the 2040s is 0.1 °C lower than that in the 2010s, while in the 2090s it is 0.3 °C lower than in the 2010s, which can increase the prevalence of heat-related diseases. The hottest locations in the PRD in both daytime and nighttime were Guangzhou and Foshan in the 2010s, but the hot area (denoted by dots) is expected to considerably expand in the future decades. The extent and intensity of this expansion will become highly severe by the 2090s, with 60% of the land area reaching a mean hourly temperature of more than 33 °C in the daytime and even more regions (79%) reaching a nighttime mean hourly temperature of more than 28 °C. Compared with the 2010s, the average spatial coverage of this hot area in the 2040s is 4 and 8 times larger in the daytime and nighttime, respectively. For the 2090s, the extent is 8 and 13 times larger in the daytime and nighttime, respectively.

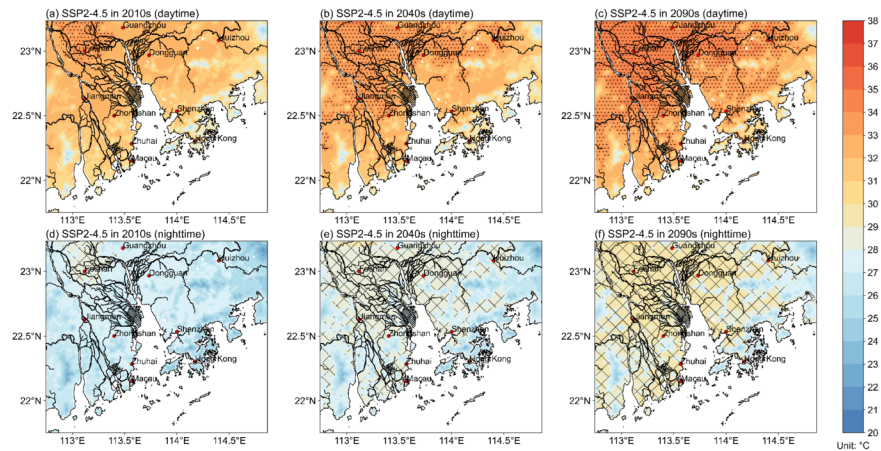


Fig. 2. (a)–(c) Daytime and (d)–(f) nighttime mean 2 m temperatures in the SSP2-4.5 scenario in the 2010s, 2040s, and 2090s. Dotted and slashed areas represent areas with temperatures more than 33 °C (first row) and 28 °C (second row) respectively. Red points indicate major cities and their names in the PRD.

Fig. 3 shows the daytime and nighttime hourly mean 2 m temperature in the 2040s and 2090s in the SSP1-2.6 and SSP5-8.5 scenarios. The spatial patterns among the scenarios do not vary considerably in the 2040s because the CO₂ emission levels in all scenarios will continue to rise until the mid-century (IPCC 2021). However, the situation in SSP1-2.6 is different from those in the other two scenarios in the 2090s. The SSP1-2.6 scenario is projected to achieve carbon neutrality after 2050, resulting in a less intense heat profile in the PRD during the 2090s compared to the 2040s. This is characterized by a decrease in daytime and nighttime temperatures by -0.3 °C and -0.2 °C respectively, along with a reduction in the size of hot areas (-10% and -7% for daytime and nighttime respectively).

On the other hand, the situation is pessimistic for the worst-case scenario, SSP5-8.5. In the 2090s, the daytime and nighttime hourly mean 2 m temperature will increase to 34.6 °C and 30.3 °C, respectively. The mean state of most locations in the PRD will even exceed the current local extreme thresholds for health cautions. In the 2090s, it is projected that over 86% and 96% of land areas will experience daytime and

nighttime hourly mean 2 m temperatures exceeding 33 °C and 28 °C, respectively. Only a few areas with elevated terrain height are expected to fall below these temperature thresholds.

To examine the impact of urbanization on temperature simulation, we calculated the mean temperature of persistent rural and rural-to-urban grid cells under SSP2-4.5. Grid cells other than urban and water bodies are classified as rural grid cells because they share similar characteristics of agricultural activities, natural vegetation, open spaces, and lower population densities. Persistent rural grids refer to the grid cells that remains rural from the 2010s to the 2040s, while rural-to-urban grid cells refer to the cells that transition from rural to urban between these periods. Synoptic systems mainly affect the temperature change of persistent rural grid cells from the 2040s to 2090s, while both synoptic systems and land use change affect the temperature of rural-to-urban grid cells in the same periods. The temperature difference between persistent rural and rural-to-urban grid cells in the 2040s and 2090s compared to the 2010s can be attributed to the impact of land use change on temperature simulation. There are a total of 1572 grid cells changing from rural to urban in the 2040s. The mean 2 m temperature of persistent rural grid cells in the 2010s, 2040s, and 2090s are 28.11 °C, 28.89 °C, and 29.72 °C, respectively. For rural-to-urban grid cells, the mean 2 m temperature was 28.87 °C, 30.27 °C, and 31.11 °C in same periods. The grid cells that underwent urbanization had a larger mean 2 m temperature in the 2010s than those persistent rural grids, and they will experience a greater temperature increase in the 2040s, and 2090s. The temperature increases for persistent rural grid cells and rural-to-urban grid cells in the 2040s and 2090s compared to the 2010s are 0.78 °C and 1.4 °C, and 1.62 °C and 2.24 °C, respectively. Therefore, we assume the land use change contribute to 0.84 °C in both 2040s and 2090s. The contribution percentage of land use change in the 2040s is 51.9% and will reduce to 37.5% in the 2090s.

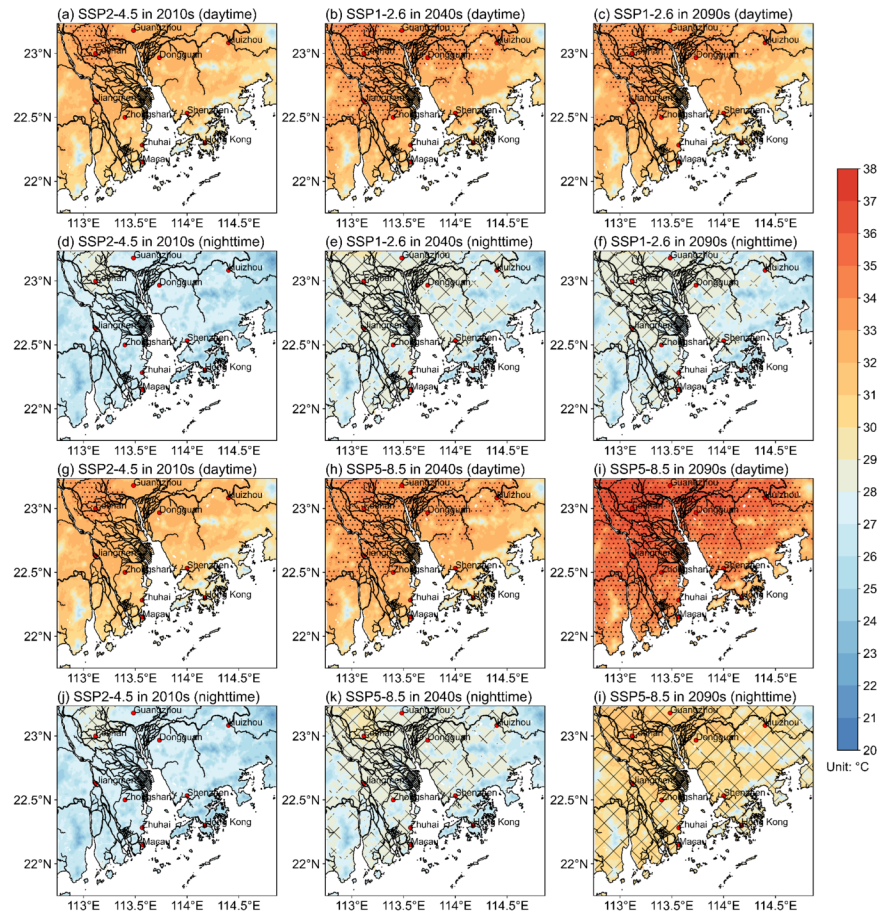


Fig. 3. Mean 2 m temperatures in the 2040s and 2090s: (b), (c) daytime and (e), (f) nighttime in the SSP1-2.6 scenario; (h), (i) daytime and (e), (f) nighttime in the SSP5-8.5 scenario. Dotted and slashed areas represent areas with temperatures more than 33 °C (first and third row) and 28 °C (second and fourth row), respectively. The first column shows the values for SSP2-4.5 in the 2010s for comparison. Red points indicate major cities and their names in the PRD.

Table 2. The spatial land mean temperatures (°C) for different scenarios in the 2010s, 2040s, and 2090s. Daytime and nighttime values are shown separately.

Scenarios	SSP1-2.6		SSP2-4.5		SSP5-8.5	
	Daytime	Nighttime	Daytime	Nighttime	Daytime	Nighttime
2010s			31.54 °C	26.85 °C		
2040s	32.27 °C	27.85 °C	32.24 °C	27.77 °C	32.33 °C	27.94 °C
2090s	32.01 °C	27.67 °C	33.0 °C	28.67 °C	34.61 °C	30.28 °C

2) Probability density functions (PDFs) of 2 m temperature values

PDFs were calculated to investigate the distribution of the land hourly temperatures over different decades in different scenarios. This section focuses on the hourly 2 m temperatures over land in each scenario for current and future periods. The associated PDFs are nonparametric curves constructed through kernel density estimation and Gaussian smoothing. The vertical lines in the plots denote the statistical value of the mean of each PDF. Three statistical metrics characterizing the PDF are calculated, including the mean, variance, and skewness (Donat and Alexander 2012). Skewness measures the extent to which the distribution of temperatures is skewed, with positive values indicating a longer tail on the right side of the curve. The sign of the skewness (positive or negative) only indicates the direction of the skewness, not its magnitude. The magnitude of different distributions is determined by the absolute value of the skewness. Variance measures the spread of the distribution from the mean, with higher values indicating greater dispersion. In meteorology, positive skewness means more extreme high than low temperatures.

Fig. 4 shows the PDFs of the hourly 2 m temperature (Fig. 4 (a–c)), daily maximum 2 m temperature (T_{max}) (Fig. 4 (d–f)), and daily minimum 2 m temperature (T_{min}) (Fig. 4 (g–i)) on land in each scenario. Under SSP2-4.5, the hourly 2 m temperature distribution shifts to the hotter side of the curve with time, with mean values of 28.97 °C, 29.76 °C, and 30.6 °C for the 2010s, 2040s, and 2090s, respectively. Skewness increases over time, with values of 0.18, 0.37, and 0.35 for the same decades, indicating longer tails in high temperatures and more extreme hot temperatures in the future. The increased mean and variance in daily maximum and minimum temperature distributions have implications for extreme heat events, not only in the daytime but also at nighttime. Under SSP5-8.5, the PDF changes with time are similar to those under SSP2-4.5 but more profound. The distribution is more skewed toward the hotter side of the curve, with larger mean values, greater variance, indicating a higher likelihood of extreme hot temperatures in the future decades. In contrast, the sustainable pathway of SSP1-2.6 shows a decrease in mean values of hourly 2 m temperature, daily maximum, and minimum temperature in the 2090s compared to the 2040s. The skewness of hourly 2 m temperature in the 2090s is smaller than that in the 2040s, with values of 0.28 and 0.37, respectively. This suggests a shorter tail in the distribution of high temperatures in the 2090s. The magnitude of negative skewness of daily maximum and minimum temperatures in the 2090s is larger than that in the 2040s, implying a longer tail on the colder side of the curve and a reduced likelihood of extreme high temperatures in the 2090s.

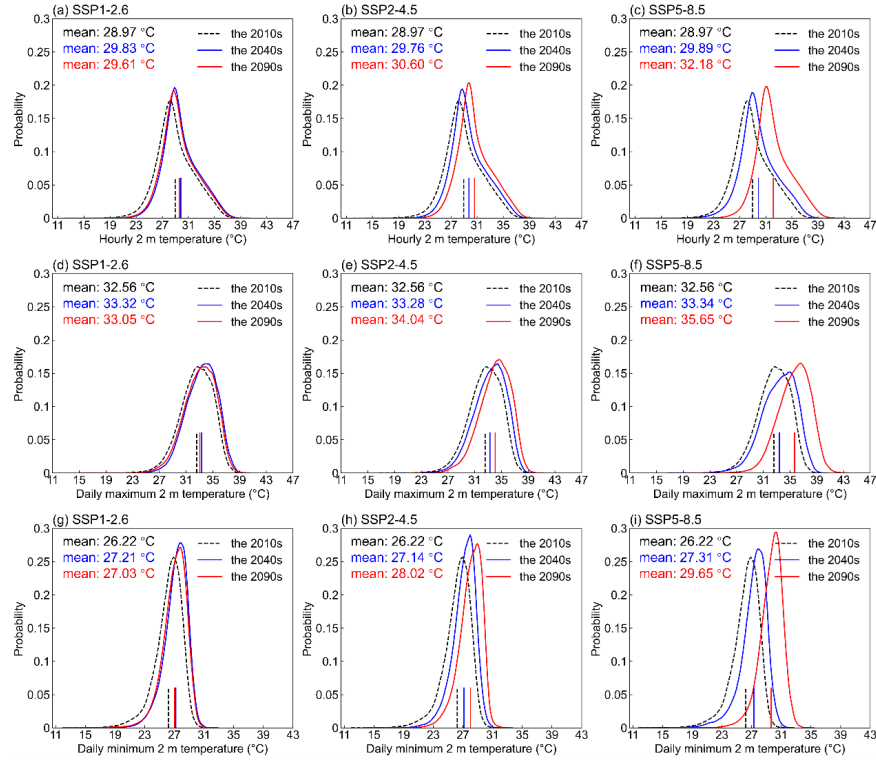


Fig. 4. (a), (b), (c) Probability density function (PDF) of hourly 2 m temperature on land in the SSP1-2.6, SSP2-4.5, and SSP5-8.5 scenarios. (d), (e), (f) PDF of daily maximum 2 m temperature on land in the SSP1-2.6, SSP2-4.5, and SSP5-8.5 scenarios. (g), (h), (i) PDF of daily minimum 2 m temperature on land in the SSP1-2.6, SSP2-4.5, and SSP5-8.5 scenarios.

Fig. 5 is a reconfigured version of Fig. 4 to compare different scenarios in each decade. The shapes of the PDFs of different scenarios appear similar in the 2040s (indicated by similar values of the variance and skewness), and the mean values are similar as well. However, with the accumulation effect of the differences among different scenarios, which include the socioeconomic assumptions, levels of climate mitigation, and air pollution controls, significant variation is observed across different scenarios in the 2090s (IPCC 2021).

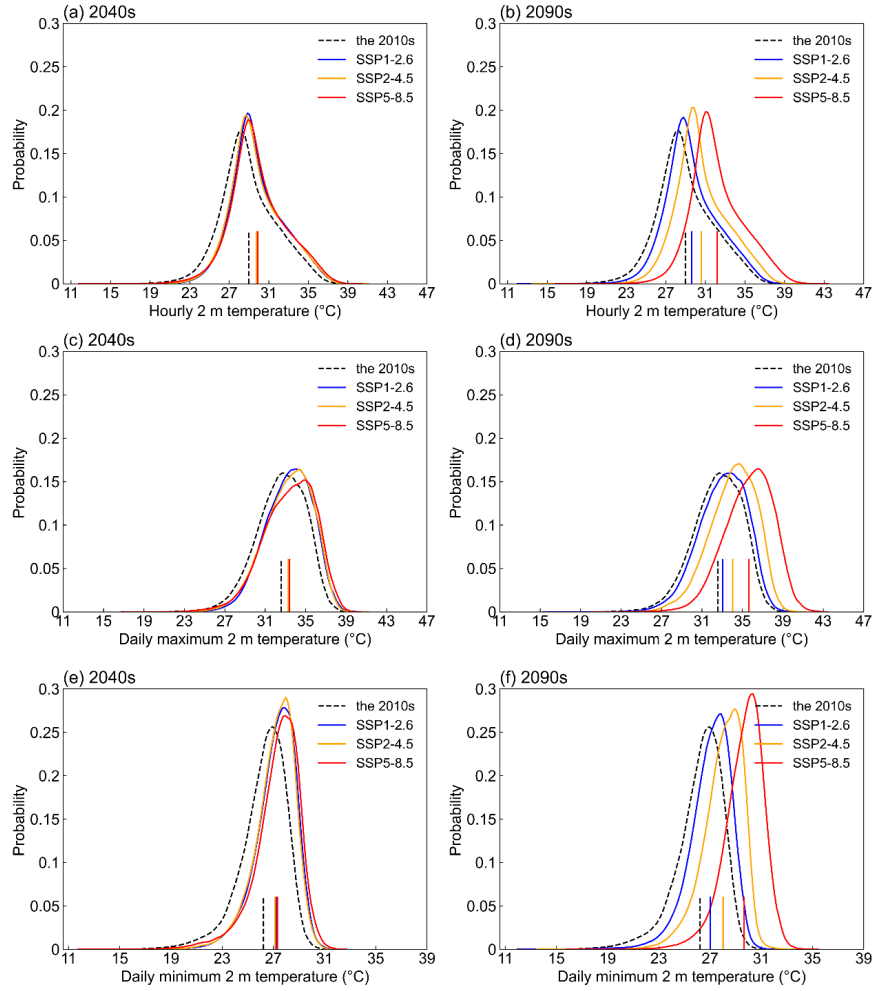


Fig. 5. (a), (b) PDF of hourly 2 m temperature on land in each scenario in the 2040s and 2090s. (c), (d) PDF of daily maximum 2 m temperature on land in each scenario in the 2040s and 2090s. (e), (f) PDF of daily minimum 2 m temperature on land in each scenario in the 2040s and 2090s.

b. Mean state of heatwave metrics for the PRD

Heatwave metrics (HDF, HWD, and HWT) were calculated for the land area of the Pearl River Delta (PRD). The PRD experienced an average of 56 very hot days in the summer during the 2010s, and this number is projected to increase to over two months in the 2040s under different scenarios (Fig. 6). By the 2090s, the differences among scenarios become more pronounced. If a more aggressive GHG emission reduction scenario is adopted, the number of very hot days is expected to decrease by 9%, reaching 65 in the summer of the 2090s compared to the 2040s. Conversely, under SSP2-4.5 and SSP5-8.5 scenarios, the number of very hot days will continue to increase after the 2040s, by 25% and 60%, respectively.

On average, heatwave events lasted for six days during the 2010s. In the 2040s, mean HWD is expected to increase by two to three days in different scenarios, while the intensity is expected to increase by 0.2°C to 0.4°C. In the worst-case scenario in the 2090s, a heatwave event in the PRD could last for 23 days, which is three times longer than that in the 2010s, and the mean daily maximum temperature could reach 36°C.

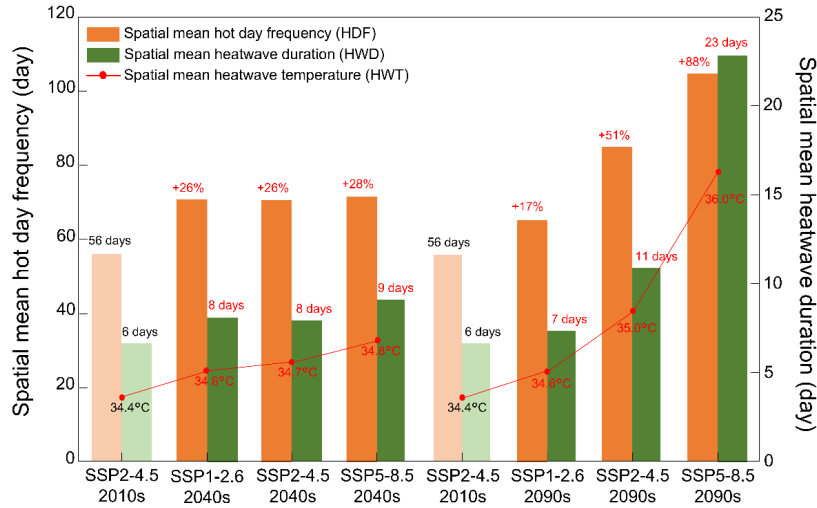


Fig. 6. Hot day frequency (HDF), daytime heatwave duration (HWD), and daytime heatwave temperature (HWT) spatially averaged over the land of PRD in different scenarios for different decades. The values are compared with the data for the SSP2-4.5 scenario for the 2010s denoted by lighter color bar.

c. Spatial analysis of heatwave metrics

The spatial patterns of the aforementioned heatwave metrics were plotted to illustrate future heatwave distribution in the PRD. Sea areas are masked out from the spatial plots to highlight the land information. All the analyses in this section are based on the SSP2-4.5 scenario, an intermediate scenario in which the social, economic, and technological trends do not change significantly from historical patterns.

In the 2010s, coastal areas had fewer very hot days than inland areas, and rural areas had fewer very hot days than urban areas. For the 122 days in the experiment period, only 9.9% of land area experienced more than 90 very hot days each summer in the 2010s. This value will increase to 41.2% and 63.9% of land in the 2040s and 2090s, respectively. In other words, in the 2090s, following the current trend, approximately 64% of the land area will suffer from high temperatures for over three months every summer, with 12% of the land area facing more than 110 very hot days, which is almost every summer day. Fig 7(a)–(c) indicate that the areas of Guangzhou, Foshan, Jiangmen, and Dongguan are at highest risk of extreme heat events, both currently and in the future due to their location farther from the coast, higher latitude, and increased urbanization. Climate change and the expansion of urban areas are projected to exacerbate this trend in the coming decades. Our results further show that urban grid cells surrounded by other urban grid cells experience higher 2 m temperatures (0.84 °C in the 2010s and 1.06 °C in the 2040s) than those surrounded by rural grid cells, with this effect expected to be more pronounced in the future due to continued urbanization. Fig. 7(d) and 7(e) show the differences in the HDFs between the 2040s and 2010s and those between the 2090s and 2010s. The greatest increase in the HDF corresponds to coastal areas in 2090s. This increase is not significant in the 2040s, which indicates that coastal areas will mostly become more vulnerable to such events at the end of the century.

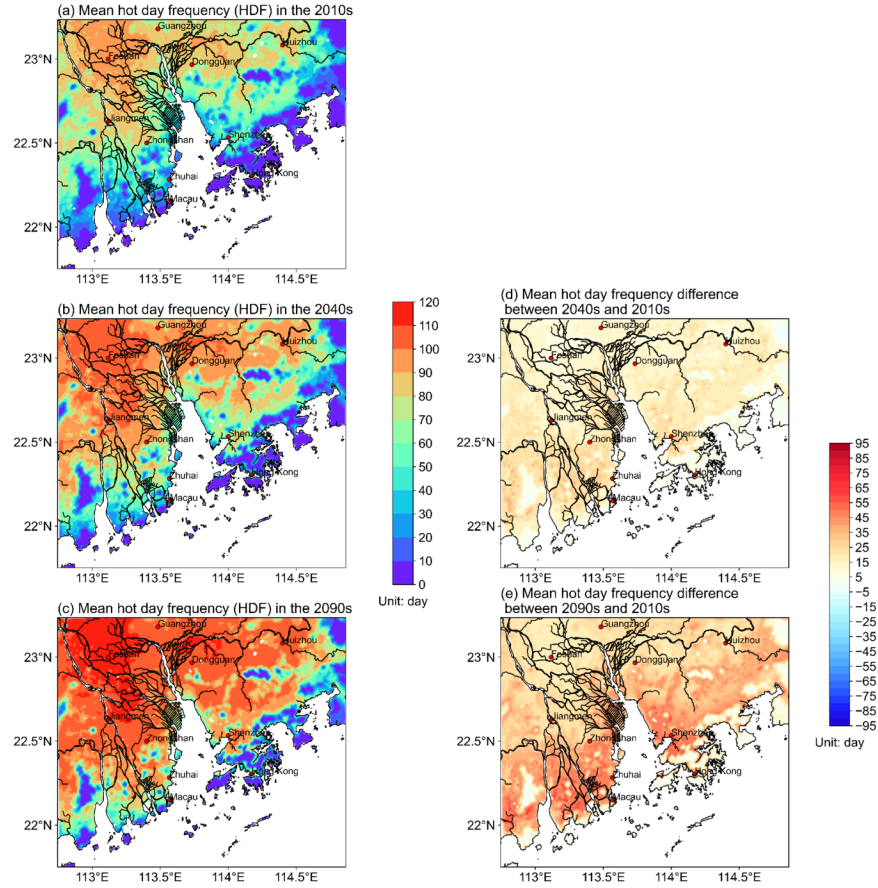


Fig. 7. (a), (b), (c) Spatial plot of mean summer hot day frequency (HDF) in the 2010s, 2040s, and 2090s. (d), (e) Spatial plot of the differences in the mean summer hot day frequency between the 2040s and 2010s and those between the 2090s and 2010s. All figures correspond to the SSP2-4.5 scenario.

In the 2010s, on average, heatwave events lasted no more than two weeks. In the 2040s, the largest HWD will increase to 15 days (Fig. 8 (b)). In the 2090s, several areas in Guangzhou and Foshan may experience heat waves lasting up to 22 days (Fig. 8 (c)). Despite the increase in the HDF, the HWD in several rural and coastal areas may decrease by 1–3 days in the 2040s. However, in the 2090s, fewer areas will experience a reduction in the HWD. Foshan is expected to have the most prolonged heatwaves, along with the largest increase in the HWD (5.5 and 13.9 days in the 2040s and 2090s, respectively). Despite a substantial increase in the number of individual very hot days (HDF) in coastal areas during the 2090s, our analysis shows that the greatest increase in consecutive very hot days (HWD) is expected to occur in Foshan and Jiangmen, due to their location farther from the coast and increasing urbanization.

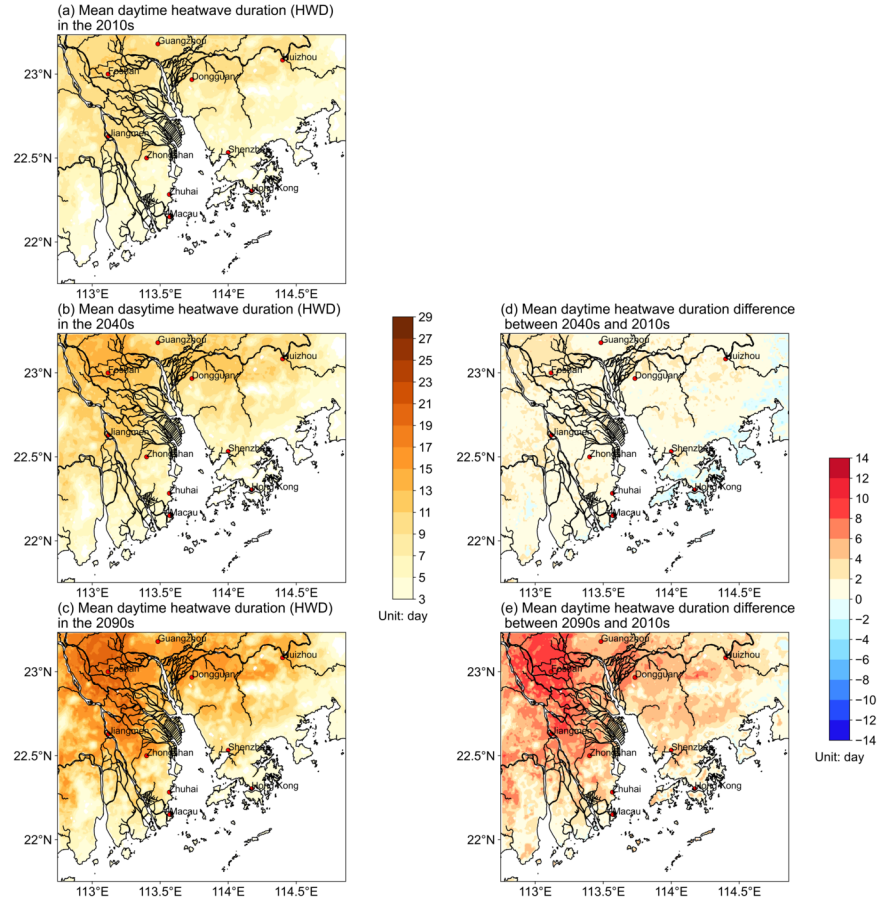


Fig. 8. (a), (b), (c) Spatial plot of mean summer daytime heatwave duration (HWD) in the 2010s, 2040s, and 2090s. (d), (e) Spatial plot of the differences in the mean summer daytime heatwave duration between the 2040s and 2010s and those between the 2090s and 2010s. All figures correspond to the SSP2-4.5 scenario.

Fig. 9 shows the mean daily maximum 2 m temperature during a heatwave. Blank areas mean that no heatwaves occur in these locations. In the 2010s, when a heatwave occurs in coastal areas, the daily maximum temperature ranges between 33 °C and 34.6 °C, lower than that in the inland areas. In the PRD, Foshan is expected to have the most intense heatwaves with the heatwave intensity reaching 35.9 °C and 36.4 °C in the 2040s and 2090s, respectively. The coastal hotspots in Fig. 9 (e), which display the difference in mean summer daytime heatwave intensity between the 2090s and the 2010s, are primarily caused by several, strong heatwave events that occurred in the 2090s which were rare in the 2010s (Fig. S12–S13). Coastal regions, which may have been accustomed to milder climates, are now more vulnerable to once-in-ten-year heatwaves because of climate warming, despite their proximity to the sea that should have provided some protection.

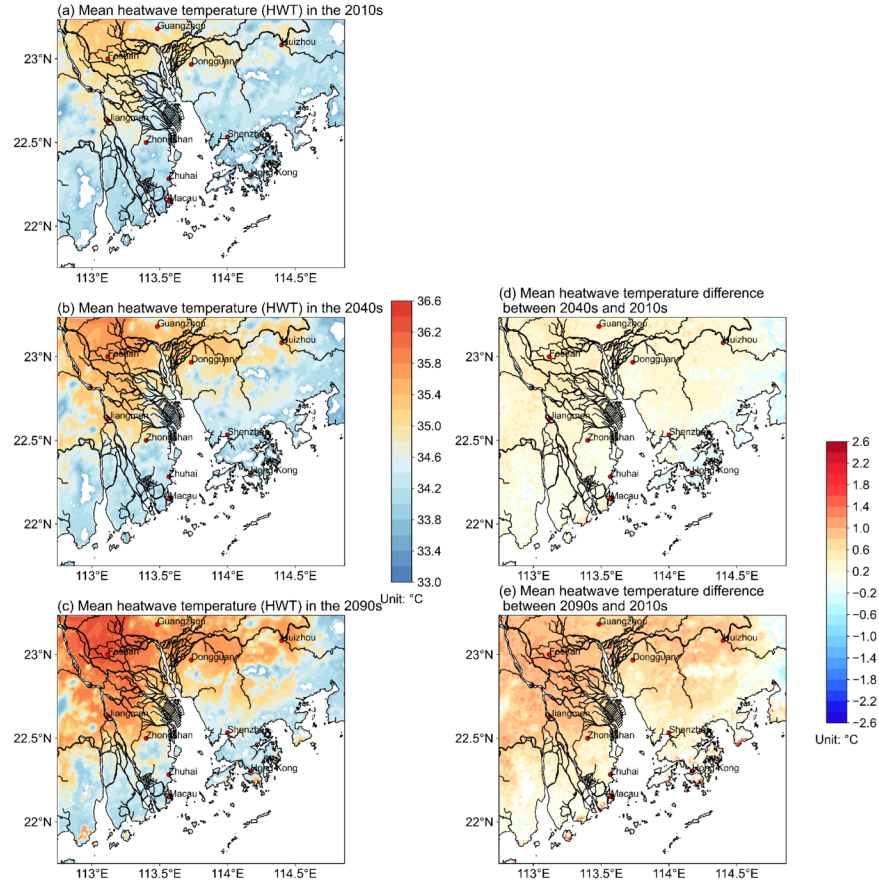


Fig. 9. (a), (b), (c) Spatial plot of mean summer daytime heatwave temperature (HWT) in the 2010s, 2040s, and 2090s. (d), (e) Spatial plot of the differences in the mean summer daytime heatwave temperature between the 2040s and 2010s and those between the 2090s and 2010s. All figures correspond to the SSP2-4.5 scenario.

The nighttime heatwave metrics were also evaluated because consecutive hot nights may pose a more significant threat to human health than very hot days. Lower temperatures at night typically allow people to recover from the daytime heat, and the occurrence of hot nights can reduce this effect, which may lead to excess death tolls (Kovats and Hajat 2008). Moreover, if consecutive very hot days occur with consecutive hot nights, the health impacts may be more severe than those associated with solely consecutive hot days or consecutive hot nights (Thomas et al. 2020). Among the human population, females and the elderly are more vulnerable to extremely hot weather (Wang et al. 2021). Fig. 10 displays the spatial patterns of the number of very hot nights (HNF) across different decades. In the 2010s (Fig. 10 (a)) rural areas had fewer than 10 very hot night. As urbanization continues to expand, more regions are expected to experience more frequent hot nights in the future. The spatial pattern of HNF difference (Fig. 10 (d)) highlights urbanization as a contributor, with more rural grid cells becoming urbanized and hot spots. For the PRD, the spatial mean difference in the HNF is 21.7 and 50.9 nights in the 2040s and 2090s, respectively, considerably larger than the mean difference in the HDF (14.6 and 28.7 days in the 2040s and 2090s, respectively). This increase will make it challenging for people to recover from the daytime heat at night. Compared with the spatial pattern of the HDF increase, which is concentrated in coastal areas, the HNF increase is more significant and spatially dispersed, covering most of the land in the PRD.

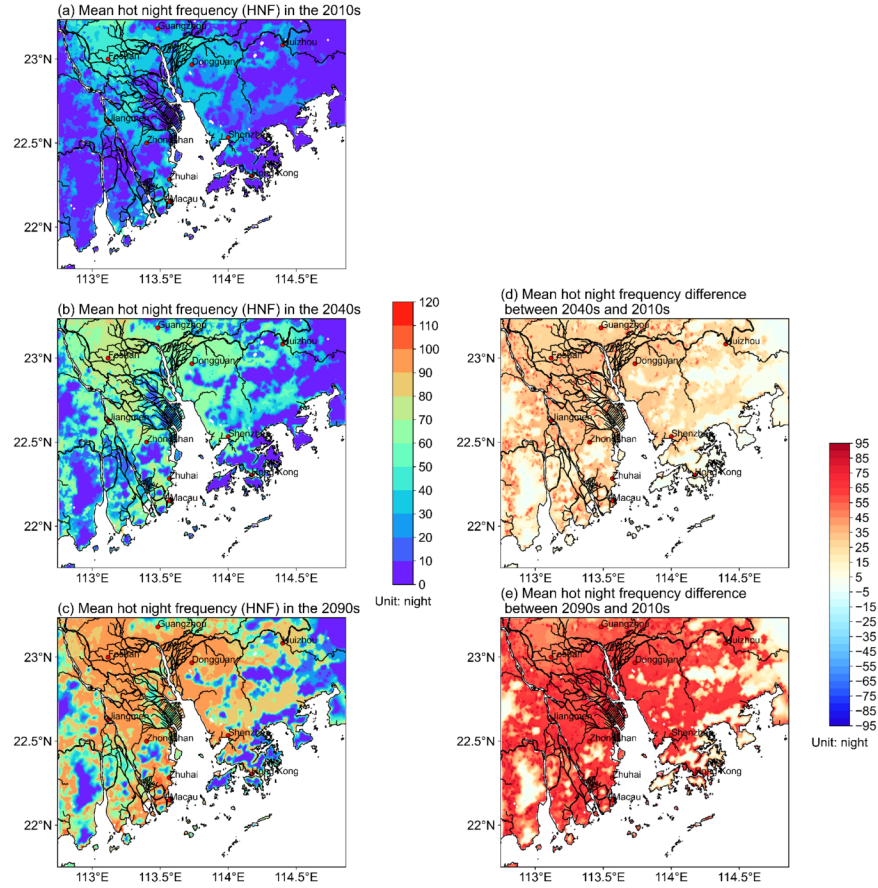


Fig. 10. (a), (b), (c) Spatial plot of mean summer hot night frequency in the 2010s, 2040s, and 2090s. (d), (e) Spatial plot of the differences in the mean summer hot night frequency between the 2040s and 2010s and those between the 2090s and 2010s. All figures correspond to the SSP2-4.5s.

The average NHD over the PRD in the 2010s, 2040s, and 2090s is 3.6, 5.1, and 7.7 nights, respectively. Although certain rural areas exhibit a lower NHD in the 2040s compared with that in the 2010s, the extent of these decreasing-NHD regions is smaller in the 2090s (Fig. 11 (d), (e)). Better urban planning and architectural design, for instance, increased natural ventilation and green areas, can help mitigate nighttime temperatures in urban areas.

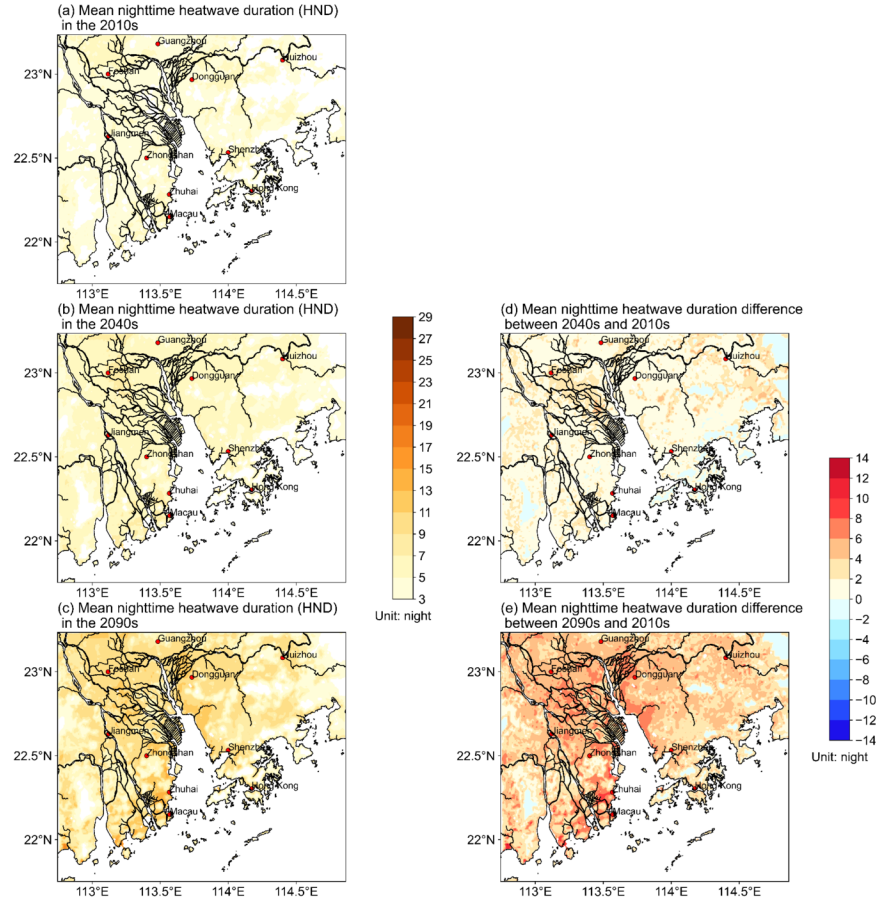


Fig. 11. (a), (b), (c) Spatial plot of mean summer nighttime heatwave duration in the 2010s, 2040s, and 2090s. (d), (e) Spatial plot of the differences in the mean summer nighttime heatwave duration between the 2040s and 2010s and those between the 2090s and 2010s. All figures correspond to the SSP2-4.5 scenario.

d. Return period analysis

Fig. 12 shows the return years in each scenario in the 2040s and 2090s relative to the once-in-a-decade event in the 2010s. The areas marked with dots and slashes correspond to return years of 0–1 and 1–2, respectively. In the 2040s, the areas with the highest extreme heat event reoccurrence are located in Guangzhou and Foshan. In the SSP1-2.6 scenario (Fig. 12 (a), (b)), the areas with return years of 0–1 and 1–2 in the 2090s is smaller than that in the 2040s. In addition, in the 2090s, Dongguan may not break the extreme temperature records corresponding to the 2010s. The spatial pattern of the return years in the SSP2-4.5 scenario is more favorable than that in SSP1-2.6 in the 2040s: the dotted and slashed areas are smaller, and more regions do not surpass the records set in the 2010s. However, in the 2090s, most locations in the PRD will suffer from the highest extreme temperature of the 2010s at least once every year or every two years. This situation is worsened in the SSP5-8.5 scenario in the 2090s, with almost every grid cell in the PRD having return year values of less than one year (Fig. 12 (f)).

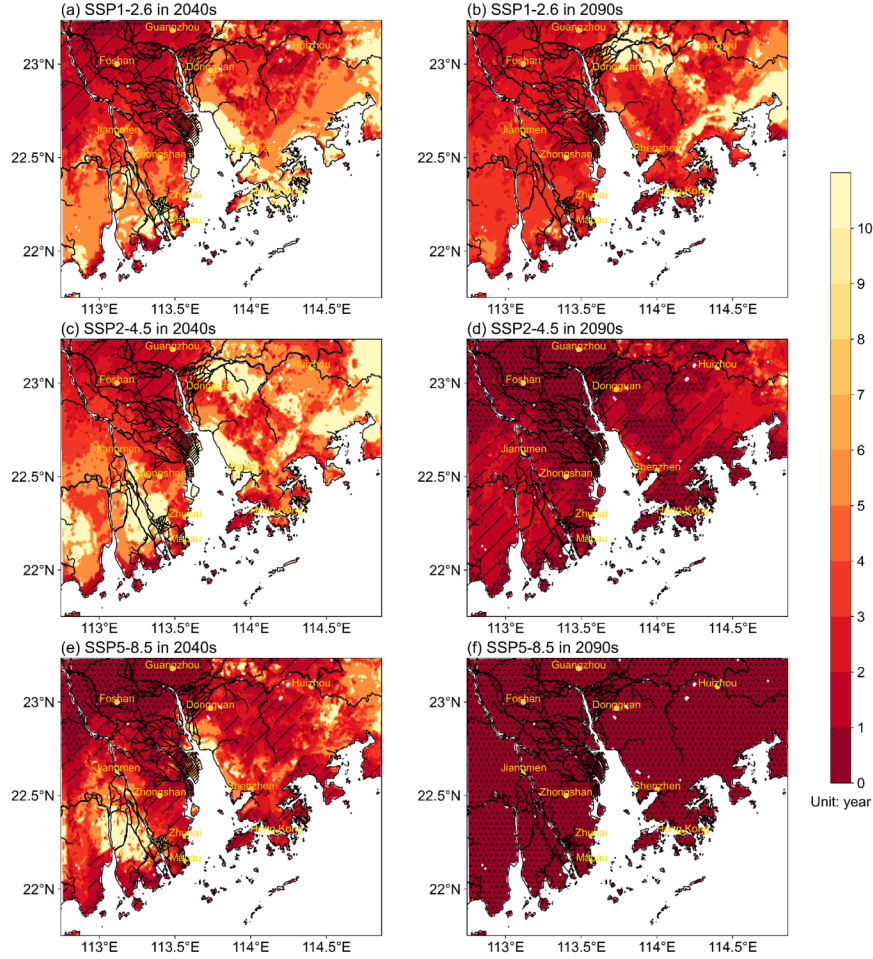


Fig. 12. Return years in the 2040s and the 2090s: (a), (b) SSP1-2.6. (c), (d) SSP2-4.5. (e), (f) SSP5-8.5. Dotted areas represent areas with return years from 0 to 1 years, and slashed areas represent areas with return years from 1 to 2 years.

Fig. 13 summarizes the increase in the frequency and intensity of extreme heat events considering the average values over the land area of the PRD. In the 2040s, an original 10-year extreme heat event will become a 4-, 4.7-, and 2.7-year event in SSP1-2.6, SSP2-4.5, and SSP5-8.5, respectively, although the increase in intensity will be similar in all three scenarios. However, by the end of the century, the differences in both the frequency and intensity increases between the intermediate pathway (SSP2-4.5) and fossil-fueled pathway (SSP5-8.5) will become substantial. Specifically, for SSP5-8.5, the return period will decrease from 10 years in the 2010s to once in each month from June to September in the 2090s.

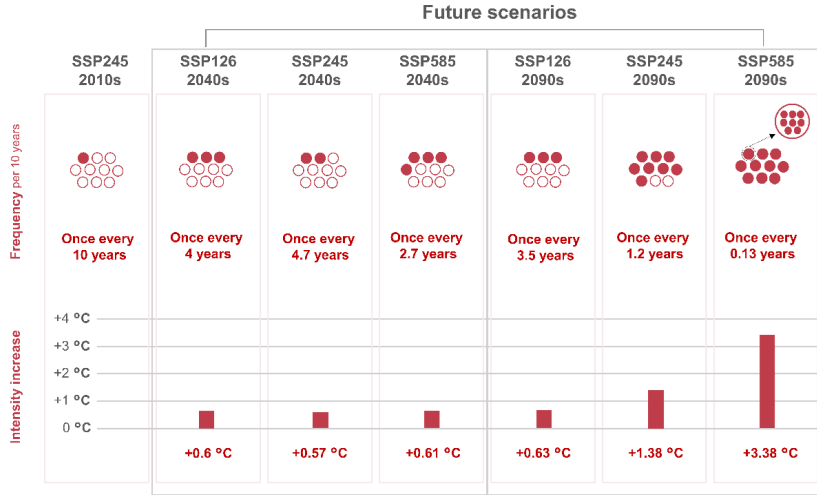


Fig. 13. Increase in the frequency and intensity of extreme heat events in different scenarios in different decades. The left column represents the reference for the 2010s. Red solid circles indicate the occurrence of the once every 10-year heatwave event in the 2010s. The red hollow circles fill the 10-year span. Therefore, in the projected scenarios, red solid circles represent the number of extreme hot events that we expect to see, reaching the level of once every 10-year events in the 2010s.

4. Conclusions

A dynamical downscaling method based on the MPI-ESM-1-2-HR of CMIP6 was used to perform a comprehensive regional climate analysis. Based on the hourly 2 m temperature data over three decades (the 2010s, 2040s, and 2090s) in three future scenarios (SSP1-2.6, SSP2-4.5, and SSP5-8.5), we explored the summer thermal environment, hot extremes, and heatwaves at present and in the future. Compared with previous studies on hot extremes, our regional simulation data were driven by the newly released global climate data. Furthermore, the future projections of land use change in the mid-century were incorporated, which is a novel addition to the research.

The results indicated that different scenarios share similar spatial patterns of the daytime and nighttime 2 m temperature in the 2040s, but the patterns significantly differ in the 2090s. SSP1-2.6, the sustainability pathway, will correspond to slightly lower daytime and nighttime temperatures in the 2090s than those in the 2040s. The opposite trends will be observed for SSP2-4.5 and SSP5-8.5, with a significant increase in the temperature and an expansion of hot areas in the 2090s. The PDFs of the 2 m temperature were analyzed to clarify the temperature distribution in the different scenarios over time. The PDFs of the 2 m temperatures and temperature extremes will shift to higher values in SSP2-4.5 and SSP5-8.5. In contrast, the PDF of the temperatures in SSP1-2.6 in the 2090s will shift to lower values.

The spatial patterns of different heatwave metrics suggest that parts of Guangdong, Foshan and Jiangmen will remain the hottest places in the PRD. Several coastal areas may experience more frequent hot extremes in the 2090s in SSP2-4.5, and some rural areas may suffer from heatwaves where the average daily maximum temperature will exceed 35°C in the 2090s. The nighttime temperature is expected to increase faster than the daytime temperature, posing a health risk to vulnerable populations especially for females and individuals aged more than 70 years. According to the heatwave analysis of the spatial mean over the PRD, although the temperatures in SSP1-2.6 will decrease in the 2090s, the extreme heat frequency and intensity will not decrease considerably, and the heatwave intensity will remain the same as that in the 2040s. In the other two scenarios, the extreme heat frequency and intensity will keep increasing in the 2040s and 2090s.

Through this research, we hope to incentivize policymakers to implement appropriate mitigation measures

and urban planning strategies to ensure people’s comfort. Considering different future climate outcomes, different social infrastructure sectors may be equipped to better prepare for the future. Moreover, the outcomes from the worst-case scenario may serve as an alert for people to adopt more sustainable lifestyles.

This research has certain limitations. Although the urban surface characteristics were considered, the anthropogenic heat flux was not considered. The definition of heatwaves used in our research allows for the possibility of overlapping dates for warm nights and warm days. This aspect of the definition may limit our ability to differentiate different types of heatwaves (daytime heatwave, nighttime heatwave, daytime-nighttime compound heatwave) and mask important signals associated with the specific mechanisms driving heatwaves in the PRD (Thomas et al. 2020; Wu and Luo 2020; Luo et al. 2022). Moreover, several studies also highlighted that the daytime- and nighttime compound heatwaves may impact human health more than solely daytime and nighttime heatwaves (Wang et al. 2021).

Acknowledgments.

We appreciate the assistance of the Hong Kong Observatory (HKO), which provided the meteorological data. The work described in this paper was supported by a grant from the Research Grants Council of the Hong Kong Special Administrative Region, China (Project Nos. AoE/E-603/18, C7041-21GF, R4046-18, and T31-603/21-N), the Guangdong-Hongkong-Macau Joint Laboratory Grant GDST20IP05, and National Natural Science Foundation of China Grant 42007203.

Data Availability Statement.

The CMIP6 large-scale climate dataset is available at <https://esgf-data.dkrz.de/search/cmip6-dkrz/>. The ECMWF Reanalysis data version 5 (ERA5) used for bias correction is available at <https://www.ecmwf.int/en/forecasts/datasets/reanalysis-datasets/era5>. The downscaled WRF output files, observation data, and other processed data files are preserved at Zenodo Repository <https://doi.org/10.5281/zenodo.7206739>. The workflow and scripts for plotting are available at Zenodo Repository <https://doi.org/10.5281/zenodo.7207845>.

REFERENCES

- Adachi, S. A., and H. Tomita, 2020: Methodology of the Constraint Condition in Dynamical Downscaling for Regional Climate Evaluation: A Review. *J. Geophys. Res. Atmos.* , **125** , <https://doi.org/10.1029/2019JD032166>.
- Bechtel, B., and Coauthors, 2015: Mapping local climate zones for a worldwide database of the form and function of cities. *ISPRS Int. J. Geo-Information* , **4** , 199–219, <https://doi.org/10.3390/ijgi4010199>.
- Bhautmage, U. P., J. C. H. Fung, J. Pleim, and M. M. F. Wong, 2022: Development and Evaluation of a New Urban Parameterization in the Weather Research and Forecasting (WRF) Model. *J. Geophys. Res. Atmos.* , **127** , <https://doi.org/10.1029/2021JD036338>.
- Camargo, S. J., 2013: Global and regional aspects of tropical cyclone activity in the CMIP5 models. *J. Clim.* , **26** , 9880–9902, <https://doi.org/10.1175/JCLI-D-12-00549.1>.
- Chan, E. Y. Y., W. B. Goggins, J. J. Kim, S. Griffiths, and T. K. W. Ma, 2011: Help-seeking behavior during elevated temperature in Chinese population. *J. Urban Heal.* , **88** , 637–650, <https://doi.org/10.1007/s11524-011-9599-9>.
- Chavaillaz, Y., P. Roy, A. I. Partanen, L. Da Silva, É. Bresson, N. Mengis, D. Chaumont, and H. D. Matthews, 2019: Exposure to excessive heat and impacts on labour productivity linked to cumulative CO2 emissions. *Sci. Rep.* , **9** , 1–11, <https://doi.org/10.1038/s41598-019-50047-w>.
- Chen, G., J. Xie, W. Li, X. Li, L. C. Hay Chung, C. Ren, and X. Liu, 2021: Future “local climate zone” spatial change simulation in Greater Bay Area under the shared socioeconomic pathways and ecological control line. *Build. Environ.* , **203** , 108077, <https://doi.org/10.1016/j.buildenv.2021.108077>.

- Chen, H., J. Sun, W. Lin, and H. Xu, 2020: Comparison of CMIP6 and CMIP5 models in simulating climate extremes. *Sci. Bull.* , **65** , 1415–1418, <https://doi.org/10.1016/j.scib.2020.05.015>.
- Ding, T., W. Qian, and Z. Yanb, 2010: Changes in hot days and heat waves in China during 1961-2007. *Int. J. Climatol.* , **30** , 1452–1462, <https://doi.org/10.1002/joc.1989>.
- Donat, M. G., and L. V. Alexander, 2012: The shifting probability distribution of global daytime and nighttime temperatures. *Geophys. Res. Lett.* , **39** , 1–5, <https://doi.org/10.1029/2012GL052459>.
- Ebi, K. L., and Coauthors, 2021: Hot weather and heat extremes: health risks. *Lancet* , **398** , 698–708, [https://doi.org/10.1016/S0140-6736\(21\)01208-3](https://doi.org/10.1016/S0140-6736(21)01208-3).
- Fan, X., C. Miao, Q. Duan, C. Shen, and Y. Wu, 2020: The Performance of CMIP6 Versus CMIP5 in Simulating Temperature Extremes Over the Global Land Surface. *J. Geophys. Res. Atmos.* , **125** , 1–16, <https://doi.org/10.1029/2020JD033031>.
- Groleau, D., F. Fragnaud, and J. Rosant, Simulation of the Radiative Behavior of an Urban Quarter.
- Guo, X., J. Huang, Y. Luo, Z. Zhao, and Y. Xu, 2017: Projection of heat waves over China for eight different global warming targets using 12 CMIP5 models. *Theor. Appl. Climatol.* , **128** , 507–522, <https://doi.org/10.1007/s00704-015-1718-1>.
- Han, Y., M. Z. Zhang, Z. Xu, and W. Guo, 2022: Assessing the performance of 33 CMIP6 models in simulating the large-scale environmental fields of tropical cyclones. *Clim. Dyn.* , **58** , 1683–1698, <https://doi.org/10.1007/s00382-021-05986-4>.
- HKO, 2020: Number of Very Hot Days. Accessed 30 January 2020, https://www.hko.gov.hk/en/cis/statistic/vhotday_statistic.htm.
- Hong, S. Y., J. Dudhia, and S. H. Chen, 2004: A revised approach to ice microphysical processes for the bulk parameterization of clouds and precipitation. *Mon. Weather Rev.* , **132** , 103–120, [https://doi.org/10.1175/1520-0493\(2004\)132<0103:ARATIM>2.0.CO;2](https://doi.org/10.1175/1520-0493(2004)132<0103:ARATIM>2.0.CO;2).
- Horton, R. M., J. S. Mankin, C. Lesk, E. Coffel, and C. Raymond, 2016: A Review of Recent Advances in Research on Extreme Heat Events. *Curr. Clim. Chang. Reports* , **2** , 242–259, <https://doi.org/10.1007/s40641-016-0042-x>.
- IPCC, 2021: Climate Change 2021: The Physical Science Basis. *Contrib. Work. Gr. I to Sixth Assess. Rep. Intergov. Panel Clim. Chang.* , .
- Kovats, R. S., and S. Hajat, 2008: Heat stress and public health: A critical review. *Annu. Rev. Public Health* , **29** , 41–55, <https://doi.org/10.1146/annurev.publhealth.29.020907.090843>.
- Liu, K., 2020: A method to improve wind speed and temperature simulation results for the weather research and forecasting model by refining surface roughness length and background albedo. Hong Kong University of Science and Technology, .
- Luo, M., N. C. Lau, and Z. Liu, 2022: Different mechanisms for daytime, nighttime, and compound heatwaves in southern China. *Weather Clim. Extrem.* , **36** , 100449, <https://doi.org/10.1016/j.wace.2022.100449>.
- MacDonald R.W., Griffiths R.F., and Hall D.J., 1998: An improved method for the estimation of surface roughness of obstacle arrays. *Atmos. Environ.* , **32** , 1857–1864.
- Mlawer, E. J., S. J. Taubman, P. D. Brown, M. J. Iacono, and S. A. Clough, 1997: Radiative transfer for inhomogeneous atmospheres: RRTM, a validated correlated-k model for the longwave. *J. Geophys. Res. Atmos.* , **102** , 16663–16682, <https://doi.org/10.1029/97jd00237>.
- Müller, W. A., and Coauthors, 2018: A Higher-resolution Version of the Max Planck Institute Earth System Model (MPI-ESM1.2-HR). *J. Adv. Model. Earth Syst.* , **10** , 1383–1413, <https://doi.org/10.1029/2017MS001217>.

- Perkins, S. E., 2015: A review on the scientific understanding of heatwaves-Their measurement, driving mechanisms, and changes at the global scale. *Atmos. Res.* , **164–165** , 242–267, <https://doi.org/10.1016/j.atmosres.2015.05.014>.
- Perkins, S. E., and L. V. Alexander, 2013: On the measurement of heat waves. *J. Clim.* , **26** , 4500–4517, <https://doi.org/10.1175/JCLI-D-12-00383.1>.
- , —, and J. R. Nairn, 2012: Increasing frequency, intensity and duration of observed global heatwaves and warm spells. *Geophys. Res. Lett.* , **39** , 1–5, <https://doi.org/10.1029/2012GL053361>.
- Pleim, J. E., 2007: A combined local and nonlocal closure model for the atmospheric boundary layer. Part I: Model description and testing. *J. Appl. Meteorol. Climatol.* , **46** , 1383–1395, <https://doi.org/10.1175/JAM2539.1>.
- Robine, J. M., S. L. K. Cheung, S. Le Roy, H. Van Oyen, C. Griffiths, J. P. Michel, and F. R. Herrmann, 2008: Death toll exceeded 70,000 in Europe during the summer of 2003. *Comptes Rendus - Biol.* , **331** , 171–178, <https://doi.org/10.1016/j.crv.2007.12.001>.
- Russo, S., and Coauthors, 2014: Magnitude of extreme heat waves in present climate and their projection in a warming world. *J. Geophys. Res. Atmos.* , **119** , 12,500–12,512, <https://doi.org/10.1002/2014JD022098>.
- S.Kain, J., 2004: The Kain–Fritsch Convective Parameterization: An Update. 170–181.
- Shi, Y., C. Ren, M. Cai, K. K. L. Lau, T. C. Lee, and W. K. Wong, 2019: Assessing spatial variability of extreme hot weather conditions in Hong Kong: A land use regression approach. *Environ. Res.* , **171** , 403–415, <https://doi.org/10.1016/j.envres.2019.01.041>.
- Stewart, I. D., and T. R. Oke, 2012: Local climate zones for urban temperature studies. *Bull. Am. Meteorol. Soc.* , **93** , 1879–1900, <https://doi.org/10.1175/BAMS-D-11-00019.1>.
- Thomas, N. P., M. G. Bosilovich, A. B. Marquardt Collow, R. D. Koster, S. D. Schubert, A. Dezfuli, and S. P. Mahanama, 2020: Mechanisms associated with daytime and nighttime heat waves over the contiguous United States. *J. Appl. Meteorol. Climatol.* , **59** , 1865–1882, <https://doi.org/10.1175/JAMC-D-20-0053.1>.
- Wang, J., and Coauthors, 2021: Anthropogenic emissions and urbanization increase risk of compound hot extremes in cities. *Nat. Clim. Chang.* , **11** , 1084–1089, <https://doi.org/10.1038/s41558-021-01196-2>.
- Wang, P., J. Tang, X. Sun, S. Wang, J. Wu, X. Dong, and J. Fang, 2017: Heat Waves in China: Definitions, Leading Patterns, and Connections to Large-Scale Atmospheric Circulation and SSTs. *J. Geophys. Res. Atmos.* , **122** , 10,679–10,699, <https://doi.org/10.1002/2017JD027180>.
- Wu, J., X. Li, S. Li, C. Liu, T. Yi, and Y. Zhao, 2022: Spatial Heterogeneity and Attribution Analysis of Urban Thermal Comfort in China from 2000 to 2020. *Int. J. Environ. Res. Public Health* , **19** , <https://doi.org/10.3390/ijerph19095683>.
- Wu, X., L. Wang, R. Yao, M. Luo, S. Wang, and L. Wang, 2020: Quantitatively evaluating the effect of urbanization on heat waves in China. *Sci. Total Environ.* , **731** , 138857, <https://doi.org/10.1016/j.scitotenv.2020.138857>.
- Wu, S., and M. Luo, 2020: Local mechanisms for global daytime , nighttime , and compound heatwaves. 1–13, <https://doi.org/10.1038/s41612-023-00365-8>.
- Xie, B., J. C. H. Fung, A. Chan, and A. Lau, 2012: Evaluation of nonlocal and local planetary boundary layer schemes in the WRF model. *J. Geophys. Res. Atmos.* , **117** , 1–26, <https://doi.org/10.1029/2011JD017080>.
- Xu, Z., Y. Han, C. Y. Tam, Z. L. Yang, and C. Fu, 2021: Bias-corrected CMIP6 global dataset for dynamical downscaling of the historical and future climate (1979–2100). *Sci. Data* , **8** , 1–11, <https://doi.org/10.1038/s41597-021-01079-3>.

Yang, X., L. Ruby Leung, N. Zhao, C. Zhao, Y. Qian, K. Hu, X. Liu, and B. Chen, 2017: Contribution of urbanization to the increase of extreme heat events in an urban agglomeration in east China. *Geophys. Res. Lett.* , **44** , 6940–6950, <https://doi.org/10.1002/2017GL074084>.

Yeung, P. S., J. C. H. Fung, C. Ren, Y. Xu, K. Huang, J. Leng, and M. M. F. Wong, 2020: Investigating future urbanization’s impact on local climate under different climate change scenarios in MEGA-urban regions: A case study of the pearl river delta, China. *Atmosphere (Basel)*. , **11** , <https://doi.org/10.3390/ATMOS11070771>.